Experimental Observation of Modulational Instability in Crossing Surface Gravity Wavetrains

MDPI

Article

Experimental Observation of Modulational Instability in Crossing Surface Gravity Wavetrains

James N. Steer [1]*, Mark L. McAllister [2], Alistair G. L. Borthwick [1] and Ton S. van den Bremer [2]

[1] School of Engineering, The University of Edinburgh, King's Buildings, Edinburgh EH9 3DW, UK
[2] Department of Engineering Science, University of Oxford, Parks Road, Oxford OX1 3PJ, UK
* ton.vandenbremer@eng.ox.ac.uk

Version March 29, 2019 submitted to Fluids

Abstract: The coupled nonlinear Schrödinger equation (CNLSE) is a wave envelope evolution equation applicable to two crossing, narrow-banded wave systems. Modulational instability, a feature of the nonlinear Schrödinger wave equation, is characterized (to first order) by an exponential growth of sideband components and the formation of distinct wave pulses, often containing extreme waves. Linear stability analysis of the CNLSE shows the effect of crossing angle, θ, on MI, and reveals instabilities between $0^\circ < \theta < 35^\circ$, $46^\circ < \theta < 143^\circ$, and $145^\circ < \theta < 180^\circ$. Herein, the modulational stability of crossing wavetrains seeded with symmetrical sidebands is determined experimentally from tests in a circular wave basin. Experiments were carried out at 12 crossing angles between $0^\circ < \theta < 88^\circ$, and strong unidirectional sideband growth was observed. This growth reduced significantly at angles beyond $\theta \approx 20^\circ$, reaching complete stability at $\theta = 30 - 40^\circ$. We find satisfactory agreement between numerical predictions (using a time-marching CNLSE solver) and experimental measurements for all crossing angles.

Keywords: Surface waves, crossing seas, modulational/Benjamin-Feir instability, coupled nonlinear Schrödinger equation (CNLSE), experiments.

1. Introduction

Crossing-seas, in which waves travel in multiple directions, have been identified as an important challenge to offshore operations and linked to an increased probability of extreme waves [1,2]. In addition to specific environmental forcing such as wind or (sudden) changes in bathymetry, two important mechanism play a role in the formation of so-called rogue waves in the ocean, namely random dispersive focusing enhanced by weak bound-wave nonlinearity and modulational instability [3–6]. Herein, we contribute to the understanding of extreme waves in crossing seas by reporting on an experimental study of modulational instability in waves crossing at angles between $0^\circ < \theta < 88^\circ$.

For long-crested or unidirectional seas, it is well established that weakly nonlinear regular wavetrains in sufficiently deep water rapidly evolve into pulses of wave groups through modulational instability (MI) [7,8]. Extreme waves can form within such groups, making MI a topic of considerable interest in the context of rogue wave events. The nonlinear Schrödinger equation (NLSE) provides the simplest mathematical framework for studying MI, and permits unstable solutions including breathers and plane Stokes waves [9,10]. Breather waves are characterized by a sudden increase in amplitude of initially regular waves to either three or five times their initial value [11,12], and provide close approximations to rogue waves in long-crested seas. However, experimentally, breather waves are particularly sensitive to initial conditions, which must be specified precisely for the waves to attain maximum amplitude [13]. In the case of the Peregrine breather, an extreme wave occurs only once during the evolution process. Conversely, the unstable regular Stokes wave seeded with sideband components to the carrier has periodic modulations that grow, facilitating straightforward

measurement of wavetrain stability, such as in the seminal paper by Lake et al. [14]. In this idealized problem, energy is returned from the sidebands to the carrier wave at later times, leading to periodic modulation and demodulation on very long time scales known as Fermi–Pasta–Ulam recurrence [15–17].

Although extensively studied both theoretically and experimentally in one dimension, the applicability of 1D NLSE to the open ocean is limited by the equation's unidirectionality. In the open ocean, waves may be created from multiple sources, interact, and cross at an angle. As derived by Onorato et al. [18] from the 2D+1 Zakharov equation [19], the coupled nonlinear Schrödinger equation (CNLSE) is a system of nonlinear wave equations describing the interaction of two narrow-banded weakly nonlinear wave systems propagating at an angle (see also [20]). The CNLSE enables both MI and crossing effects to be explored simultaneously. By invoking the assumptions of symmetrical propagation about the x-axis at angle $\pm\theta$ and shared group velocity along the x-axis, the CNLSE simplifies and readily lends itself to linear stability analysis. The results define both low angle and high angle instability regions separated at $\theta = 35.26^\circ$ and $\theta = 144.74^\circ$ (see also [21]). Discussions concerning linear stability of CNLSE and the effect of the changing values of CNLSE coefficients with crossing angle have highlighted increased amplification factors but decreased growth rates of breather and soliton solutions in crossing seas for angles approaching 35.26° [22,23]. When we refer to crossing angle in this paper, we will refer to the angle θ, when two waves cross at $\pm\theta$ (so that the angle of bisection is 2θ).

Laboratory experiments by Toffoli et al. [24] have measured the long-term statistical behaviour of weakly nonlinear crossing waves up to crossing angles of 20° (see fig. 1b for these experimental angles). Numerical solutions using a higher-order spectral method were used to confirm these findings and additionally, to study crossing angles up to 90° and found increases in kurtosis for crossing angles in the range $20^\circ < \theta < 30^\circ$ [25]. Additionally, the effect of oblique sideband perturbations (of up to 37°) to plane waves propagating over finite depth have also been investigated experimentally and sideband growth was reported [24]. The existence of short crested crossing breather waves (slanted breather solutions to the 2D+1 NLSE) has also been confirmed experimentally [26].

In addition to possible MI, changes to the second-order bound waves occur when waves cross. The wave-averaged free surface, represented spectrally by second-order difference waves, is the local mean surface elevation formed by temporal averaging over the rapidly varying waves that make up the slowly varying group. Whereas a set-down of the wave-averaged free surface is expected in the absence of crossing, packets are accompanied by a set-up for sufficiently large crossing angles. This can be theoretically predicted [27–30] based on second-order interaction kernels [31–34]. A set-up has been observed in field data [35–37] and recently in detailed laboratory experiments [38]. For the Draupner wave, recorded in the North Sea on the 1st of January 1995 [39], the observation of set-up can be seen as evidence for crossing [35,40,41]. In fact, linear dispersive focusing enhanced by bound-wave nonlinearity but without MI may be sufficient to explain observations such as the Draupner wave [42,43].

Recently, a number of additional numerical studies have examined extreme waves and MI in crossing seas. Støle-Hentschel et al. [44] have shown, using numerical simulations and laboratory experiments, that a small amount of energy travelling in exactly the opposing direction can significantly reduce the kurtosis of the surface elevation. Gramstad et al. [45], using random simulations of the Zakharov equation, have found an increase in the kurtosis at crossing angles close to 50°, but even higher values for very small crossing angles, where the spectrum is unimodal, and minimum kurtosis at crossing angles close to 90°.

In this paper, we report on regular wave experiments with seeded sidebands for two crossing wavetrains in a circular wave basin. These experiments are the crossing-wave counterpart of the classical experiments by Lake et al. [14] and cover both stable and unstable regions of the (K, θ) space, through the range $0^\circ < \theta < 88^\circ$, where K is the perturbation wavenumber. We measure the growth of sidebands and compare this to results from linear stability analysis of the CNLSE, as well as numerical

solutions of this equation.

This paper is laid out as follows. First, §2 reviews the theoretical background, followed by an exposition of our experimental methodology in §3. Experimental results are presented and compared to solutions of the CNLSE in §4. Finally, conclusions are drawn in §5.

2. Theoretical background

2.1. Coupled nonlinear Schrödinger equation (CNLSE)

The coupled nonlinear Schrödinger equation (CNLSE), derived by [18] from the 2D+1 Zakharov equation [19], is a narrow-banded wave equation describing the evolution of coupled, complex wave envelopes A and B. Both wave envelopes propagate on an associated carrier wave whose properties define the CNLSE coefficients and thus (along with the initial conditions) the envelope evolution. Scaled for water waves, and under the assumption of identical but symmetrical carrier waves (about the x-axis) with distinct amplitude envelopes, the CNLSE is given, in a Cartesian coordinate system (x, y, t), by [18],

$$\frac{\partial A}{\partial t} + C_x\frac{\partial A}{\partial x} + C_y\frac{\partial A}{\partial y} - i\alpha\frac{\partial^2 A}{\partial x^2} - i\beta\frac{\partial^2 A}{\partial y^2} + i\gamma\frac{\partial^2 A}{\partial x\partial y} + i(\xi|A|^2 + 2\zeta|B|^2)A = 0, \tag{1}$$

$$\frac{\partial B}{\partial t} + C_x\frac{\partial B}{\partial x} - C_y\frac{\partial B}{\partial y} - i\alpha\frac{\partial^2 B}{\partial x^2} - i\beta\frac{\partial^2 B}{\partial y^2} - \gamma\frac{\partial^2 B}{\partial x\partial y} + i(\xi|B|^2 + 2\zeta|A|^2)B = 0, \tag{2}$$

where carrier properties, frequency ω_0; x-axis wavenumber k; y-axis wavenumber l; and absolute wavenumber $k_0 = \sqrt{k^2 + l^2}$, define the group velocities C_x and C_y along their respective axes,

$$C_x = \frac{\omega_0}{2k_0^2}k \text{ and } C_y = \frac{\omega_0}{2k_0^2}l, \tag{3a,b}$$

the linear coefficients α, β, and γ are given by,

$$\alpha = \frac{\omega_0}{8k_0^4}(2l^2 - k^2), \quad \beta = \frac{\omega_0}{8k_0^4}(2k^2 - l^2), \text{ and } \gamma = -\frac{3\omega_0}{4k_0^4}lk, \tag{4a,b,c}$$

and the nonlinear coefficients ξ and ζ by.

$$\xi = \frac{\omega_0}{2k_0}\frac{k^5 - k^3l^2 - 3kl^4 - 2k^4k_0 + 2k^2l^2k_0 + 2l^4k_0}{(k - 2k_0)k_0} \text{ and } \zeta = \frac{2\xi}{\omega_0 k_0^2}. \tag{5a,b}$$

The carrier frequency ω_0 and absolute wavenumber k_0 are related through the deep water dispersion relation, $\omega_0 = \sqrt{k_0 g}$, with g denoting the gravitational constant.

In the special case of envelopes propagating along the x-axis, a Galilean transformation into the group reference frame reduces the CNLSE to [18],

$$\frac{\partial A}{\partial t} - i\alpha\frac{\partial^2 A}{\partial X^2} + i(\xi|A|^2 + 2\zeta|B|^2)A = 0, \tag{6}$$

$$\frac{\partial B}{\partial t} - i\alpha\frac{\partial^2 B}{\partial X^2} + i(\xi|B|^2 + 2\zeta|A|^2)B = 0, \tag{7}$$

where $X = x - C_x t$. From the wave packet amplitudes, the (linear) free surface elevation is reconstructed by reintroducing the carrier waves through,

$$\eta = \mathrm{Re}\left[Ae^{i(kx+ly-\omega_0 t)} + Be^{i(kx-ly-\omega_0 t)}\right]. \tag{8}$$

2.2. Linear stability analysis

Linear stability analysis of the CNLSE reveals many properties of the equation and, using a seeded carrier solution, allows prediction of the initial sideband growth rate. Identical plane waves are admitted as solutions to (6-7) and we therefore add perturbations of infinitesimal amplitude and phase to obtain (see also [18]),

$$A = a_0(1+\delta_a)e^{-i(\omega_0 t+\delta\phi_a)} \text{ and } B = b_0(1+\delta_b)e^{-i(\omega_0 t+\delta\phi_b)}, \tag{9a,b}$$

where a_0 and b_0 are carrier amplitudes, and δ_a, δ_b, $\delta\phi_a$, and $\delta\phi_b$ are small perturbations in amplitude and phase. In this linear stability analysis, the assumed form of the sideband solutions a_δ and b_δ is,

$$a_\delta = a_{\delta,0}e^{i(\Omega t \pm Kx)} \text{ and } b_\delta = b_{\delta,0}e^{i(\Omega t \pm Kx)}, \tag{10a,b}$$

where $a_{\delta,0}$ and $b_{\delta,0}$ are the initial sideband amplitudes, K is the perturbation wavenumber, and Ω is the perturbation frequency. The relationship between K and Ω is found through linear stability analysis as [18],

$$\Omega = \pm\sqrt{\alpha K^2[(\xi(a_0^2+b_0^2+\alpha K^2) \pm \sqrt{\xi^2(a_0^2-b_0^2)^2+16\zeta^2 a_0^2 b_0^2}]}, \tag{11}$$

where it is apparent that Ω may take either real or imaginary values. Following substitution of this relationship into (10), either oscillatory (when $\Omega \in$ Re) or exponential (when $\Omega \in$ Im) behaviour can be expected.

Figure 1 presents the instability regions bounded by $K_c(\theta)$ in (K,θ)-space, where three regions of instability exist: at low angle, $0^\circ < \theta < 35^\circ$; medium angle, $46^\circ < \theta < 143^\circ$; and high angle, $145^\circ < \theta < 180^\circ$, where θ is related to the carrier wavenumbers through $\theta = \arctan(l/k)$. Figure 1a also shows where in (K,θ) space the experiments reported on herein lie, with fig. 1b showing the location of the experiments previously reported by Toffoli et al. [25]. These experiments are restricted to angles $0^\circ < \theta < 20^\circ$ and are carried out with a continuous spectrum instead of discrete sidebands, as illustrated by the horizontal lines in fig. 1b, with 85% of their energy bounded by the y-axis and the black crosses.

For unidirectional waves, MI behaves as described by the standard NLSE but with increased instability due to the presence of two carrier waves, with a consequent doubling of steepness. As the crossing angle is progressively increased, the region of instability extends further along the wavenumber axis, whereas the magnitude of the instability decreases gradually. At $\theta \approx 35.26^\circ$ (exactly, $\theta = \arctan(1/\sqrt{2})$), the low angle instability region ends, having encompassed all wavenumbers. At approximately 46°, the medium-angle instability region begins to take shape, starting close to zero wavenumber and expanding along the wavenumber axis until the crossing angle reaches approximately 143°. Finally, the high-angle region commences as a sharp boundary at approximately 145° and ends as a mirrored version of the low-angle region (with both waves travelling at 180° from the x-axis).

2.3. Characteristics of modulational instability: complex vs. simple evolution

Figure 2 presents the spectral and temporal evolution of two modulated wavetrains with different perturbation wavenumbers propagating from the initial conditions (9) with $\theta = 20^\circ$ and $a_{\delta,0} = 0.1a_0$, obtained using a numerical solver of the CNLSEs (see appendix A). The effect of MI is instantly recognizable from the increase in amplitude of the sidebands closest to the carrier wave (primary sidebands). As the primary sideband amplitudes increase, the carrier amplitude begins to decrease. Further in the evolution process, secondary sidebands appear at integer multiples of the primary sideband wavenumber. The effect of this initial stage of instability is seen in the packet amplitude in fig. 2b as a rapid increase in the group amplitude. Following the exponential sideband amplitude growth, Fermi–Pasta–Ulam (FPU) recurrence is observed. During FPU recurrence, energy is exchanged periodically between modes, and the system returns to its original state [15–17]. We note that FPU

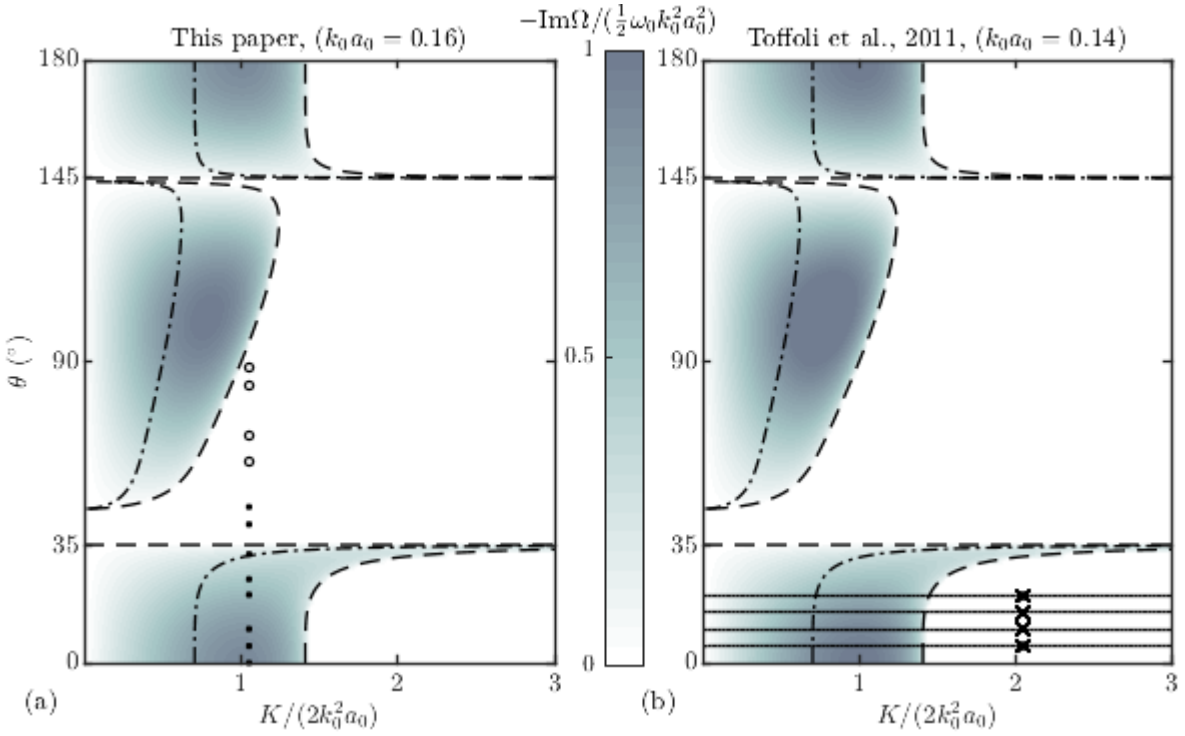

Figure 1. Surfaces showing the growth rate obtained from linear stability analysis of the coupled nonlinear Schrödinger equation (from (11)). The parameters for experiments 2a-h are indicated by dots (results presented in main text) and experiments 2i-l by open circles (results presented in appendix B). The crossing angles of experiments performed by Toffoli et al. [25] are shown as solid lines in panel b with the crosses and y-axis marking the boundary containing 85% of the spectral energy (note that the crossing angle β in Toffoli et al. [25] is equivalent to 2θ). The dashed lines indicate boundaries of stability regions, while the dot-dashed lines show the boundary between complex ($0 < K \leq K_c/2$) and simple ($K_c/2 < K < K_c$) evolution.

recurrence is a long-term behaviour, and strong MI is required to observe it in the space available in most experimental facilities.

Figure 2a and b show the wavetrain propagating with complex recurrence, whereas Figure 2c and d show simple recurrence. Complex recurrence is expected when K lies less than (or at) half way through the instability region ($K \leq K_c/2$), and primary sidebands themselves act as unstable carriers, continually spawning new sidebands. When K lies more than half way to the stability boundary ($K_c/2 < K < K_c$) new sidebands will lie in the stable region, and simple recurrence is observed.

3. Experimental methodology

3.1. Facility

The aim of our experiments was to measure sideband growth at extreme crossing angles up to 90°. In order to achieve this, all experiments were performed in the FloWave Ocean Energy Research Facility, located at the University of Edinburgh, which is capable of omnidirectional wave creation and absorption. The basin (depicted in fig. 3a and b) has a diameter of 25 m, a working depth of 2 m, and is encircled by 168 actively absorbing force-feedback wavemakers. A Cartesian coordinate system was defined with its origin at the centre of the basin. The primary direction of propagation of the waves was in the positive x direction. In crossing wave experiments, the carrier waves travelled at an angle θ from the x-axis, as defined in fig. 3a. Wave generation in the facility was controlled using software based on linear wave theory. Ten resistance type wave gauges at a spacing of 1.5 m were mounted on a gantry spanning the basin x-axis (see fig. 3b for coordinates). Wave gauges were calibrated each

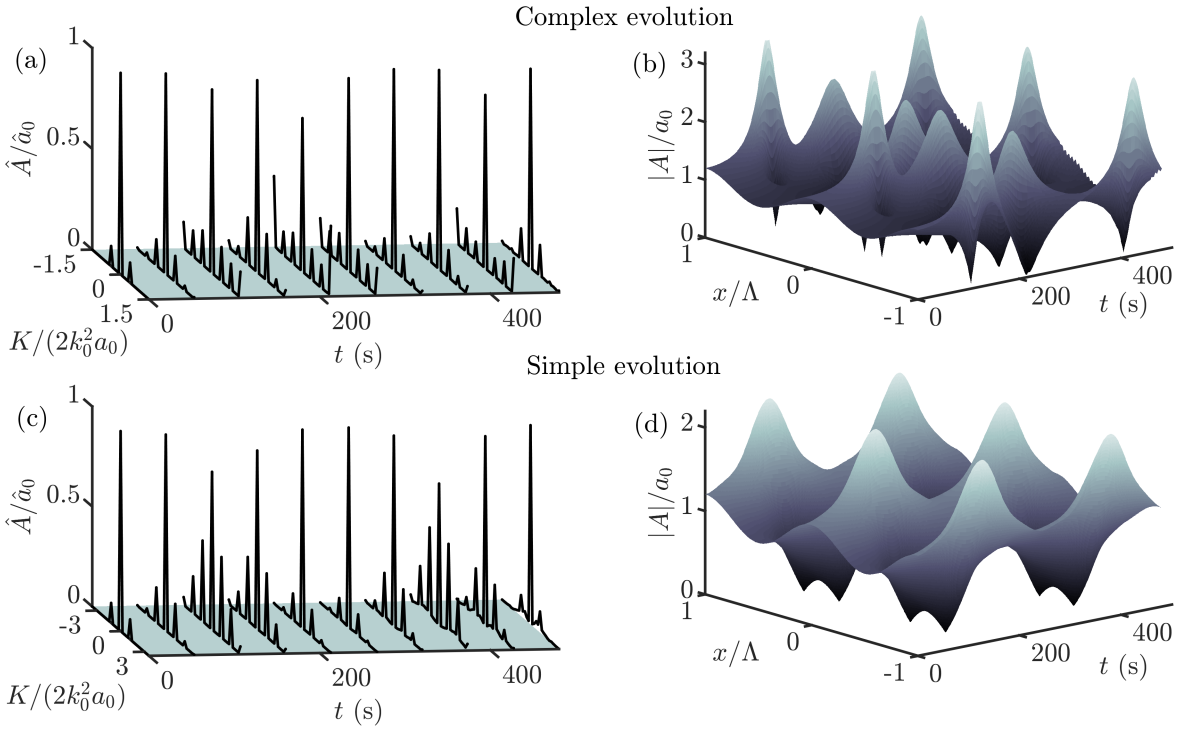

Figure 2. Spectral and temporal evolution obtained from the time-marching of the CNLSE for two unstable modulated wavetrains crossing at $\theta = 20°$. Panels a and b show complex ($0 < K \leq K_c/2$) evolution, whilst panels c and d display simple ($K_c/2 < K < K_c$) evolution.

day before tests commenced. A 20 minute settling period was imposed between each test, allowing residual basin motion to settle to an acceptable level.

3.2. Matrix of experiments

The experimental campaign was split into two parts. Part I aimed to quantify the effect of finite length crests in the facility even in the absence of seeded sidebands, which is a manifestation of the inability of a finite number of wavemakers encircling a finite-size round basin to perfectly create long-cresed waves. Part II aimed to measure the growth of frequency sidebands about carrier waves travelling at crossing angles $\pm\theta$. Crossing carrier and sideband waves only interact fully in regions of total crest overlap, and so the extent that these regions cover the chosen wave gauge locations is defined by the carrier crest length and angle. Experiments 1a-d (part I) were therefore designed to determine the effective sideband evolution region in the basin at each angle. In these experiments, a single unseeded carrier wave was propagated at the angles given in table 1 (part I).

For part I, the amplitude profiles of experiments 1a-d are presented in fig. 3c and allow estimation of the carrier crest length in the FloWave facility. Experiment 1d ($\theta = 90°$) shows that, for high angle experiments, a reasonable region in which to expect full sideband-carrier interactions occupies approximately 10 wavelengths centred about the basin origin. However, the effective length is extended significantly to more than 20 wavelengths for crossing angles up to 30°, the region of greatest interest in part II. As expected, for waves in the x-direction ($\theta = 0°$), the region covers all wave gauge locations. The results from the part I tests were interpolated in order to estimate the finite-crest effect at all crossing angles.

All experiments in part II were performed with constant values of carrier frequency, carrier frequency $f_0 = 1.5$ Hz, carrier amplitudes $a_0 = b_0 = 0.018$ m, and initial sideband amplitude $a_\delta = 0.003$ m, giving a depth parameter $k_0 d = 18$, and steepness $k_0 a_0 = 0.16$. Figure 1a shows the expected growth rates, crossing angles, and sideband wavenumbers for the part II tests. A simple system of four plane waves, consisting of two carrier waves propagating at $\pm\theta$ to the x-axis, and two

	Part I				Part II											
Expt.	1a	1b	1c	1d	2a	2b	2c	2d	2e	2f	2g	2h	2i	2j	2k	2l
θ (°)	0	30	60	90	0	5	10	20	25	32	41	47	60	68	83	88

Table 1. Experiment labels and their corresponding crossing angles for both part I (single, unseeded regular wave) and part II (seeded waves). All experiments used carrier parameters of $f_0 = 1.5$ Hz, $k_0 a_0 = 0.16$, and $k_0 d = 18$. Experiments 2a-l used sideband parameters of $K = 3.02$ m^{-1}, and $a_\delta = 0.003$ m.

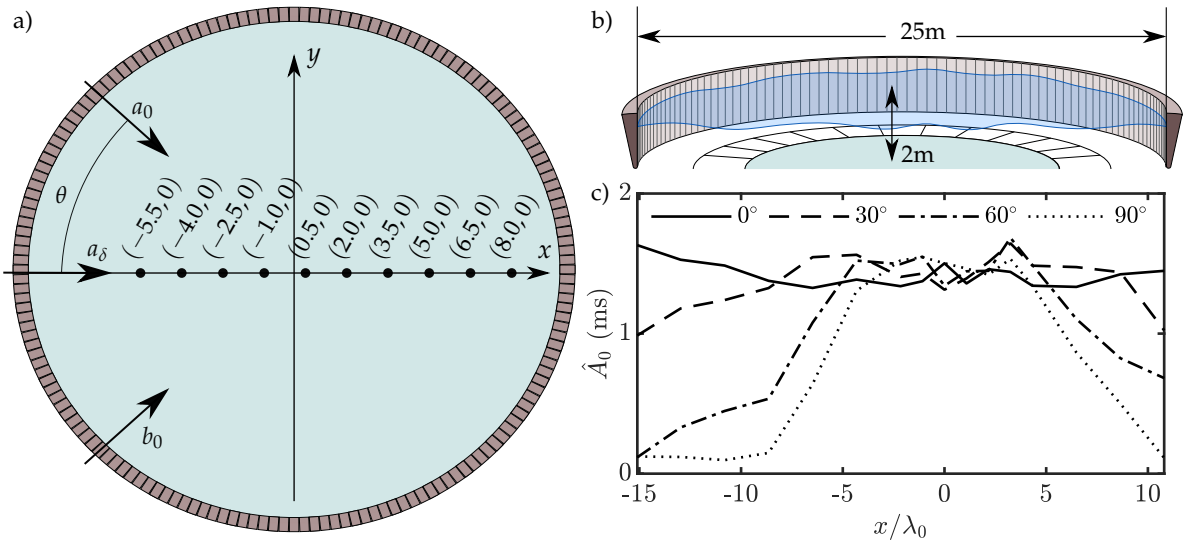

Figure 3. a: FloWave Ocean Energy Research Facility at The University of Edinburgh, showing wave gauge locations relative to the centre of the basin $(0, 0)$ (units in m) and direction of wave system components (figure adapted from [46]). **b:** Sectional view of the FloWave basin with key dimensions. **c:** Amplitude profiles of unseeded carrier waves ($f_0 = 1.5$ Hz) travelling at an angle θ and measured along the basin x-axis (part I).

sidebands propagating along the x-axis was used as input to the wave generation software. To increase the effective evolution distance and the magnitude of the instability, a relatively high carrier frequency of $f_0 = 1.5$ Hz was chosen and the carrier amplitude then calculated to give a moderate steepness of $k_0 a_0 = 0.16$, required for prominent instability but to avoid breaking. Each experiment was repeated 3 times.

3.3. Data processing

The calibrated wave gauge outputs (free surface time histories) from each experiment were band-pass filtered to eliminate higher-order and low-frequency bound waves. Reflected waves were omitted from the free surface time histories by multiplying the incident wave signal during the wavemaker start-up period by a Tukey window. This produced a quasi steady-state at each gauge (see fig. 4). The amplitude spectrum was determined at each location (see fig. 5), and the evolution of the primary sidebands (frequency components located closest to the carrier wave) used to identify MI. The true frequency of these components was determined at the first gauge location. These component amplitudes were then tracked across all the remaining wave gauges. Sideband and carrier amplitudes at the first wave gauge location were used as initial conditions for a CNLSE solver (using the Fourier, split-step method, see appendix A) and as inputs to the prediction by the linear stability analysis (11). The experimental evolution of the sidebands is compared to these experimental solutions, as well as the linear stability analysis (11) below.

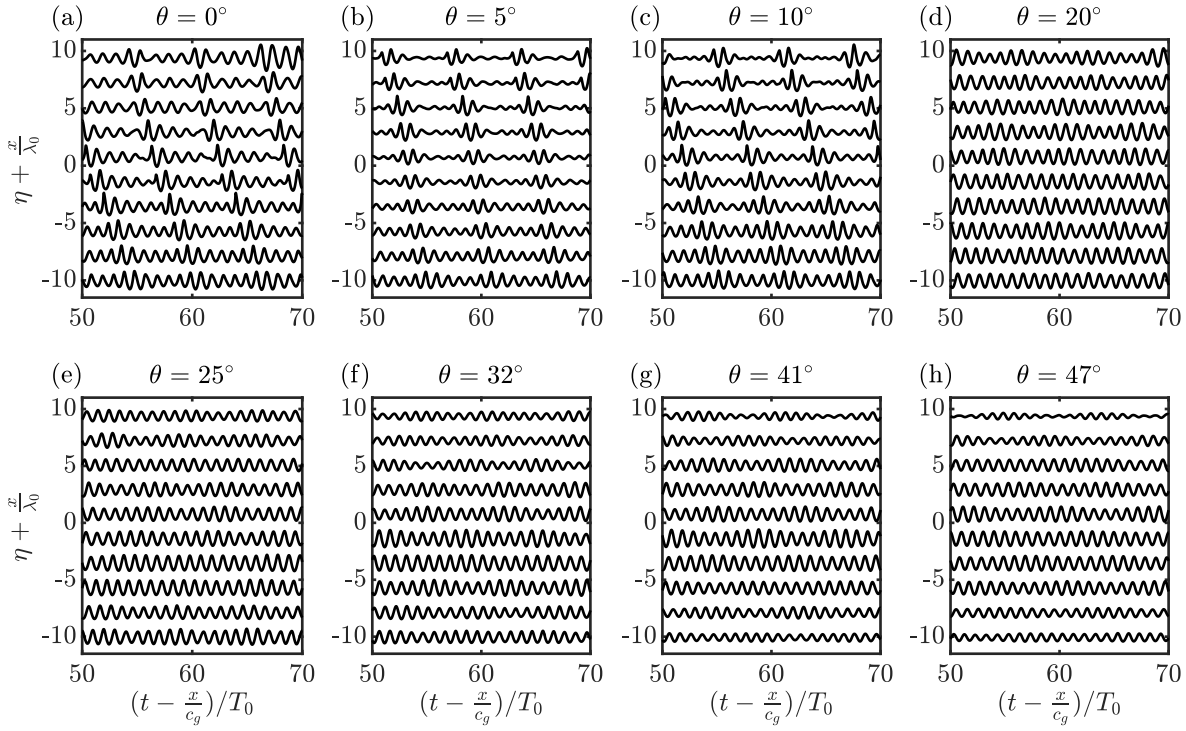

Figure 4. Measured free surface elevation time series for experiments 2a-h (part II) shifted by the linear group velocity $c_g = \sqrt{C_x^2 + C_y^2}$, with the positive vertical axis also representing increasing distance along the basin.

4. Results

Figure 6 presents the evolution of the primary sideband amplitudes of experiments 2a-l along with numerical results from the CNLSE time-marching scheme and the linear stability analysis. For brevity, only experiments 2a-h are presented (see appendix B for experiments 2j-l, which show stability, as predicted). Each experimental repeat was solved across the spatial domain using the CNLSE solver. The results of the solver were then averaged and the standard deviation across repeats was calculated. Error bars for experimental measurements and dashed lines for the numerical scheme are used to indicate one standard deviation from the mean across repeats. The carrier amplitude evolution is denoted by dark grey lines and the interpolated measurements from part I are denoted by light grey lines, indicating the region over which an unseeded carier wave can be considered of constant amplitude.

4.1. Unidirectional waves: $\theta = 0°$

The unidirectional experiment 2a, presented in fig. 6a, shows the most significant growth in sideband amplitude, with the lower sideband increasing by more than a factor of three. An increase in amplitude can also be observed in the upper sideband. The beginnings of FPU recurrence appear. The numerical solution in fig. 6a also shows significant growth and follows the average of the upper and lower sideband amplitudes well, displaying many of the same characteristics (such as FPU recurrence). However, the lower sideband grows much more quickly than the upper sideband, which is subject to initial growth followed by considerable attenuation, a feature not predicted by the NLSE but predicted in the modified NLSE [47] and commonly observed in unidirectional experiments [48].

The effect of sideband growth and MI on free surface elevation is shown by the formation of pulses in fig. 4. Extreme waves occur in these pulses when carrier crests come in phase with the group centre, as demonstrated in fig. 4a at $x/\lambda_0 \approx 3$, where a cluster of three waves has more than doubled

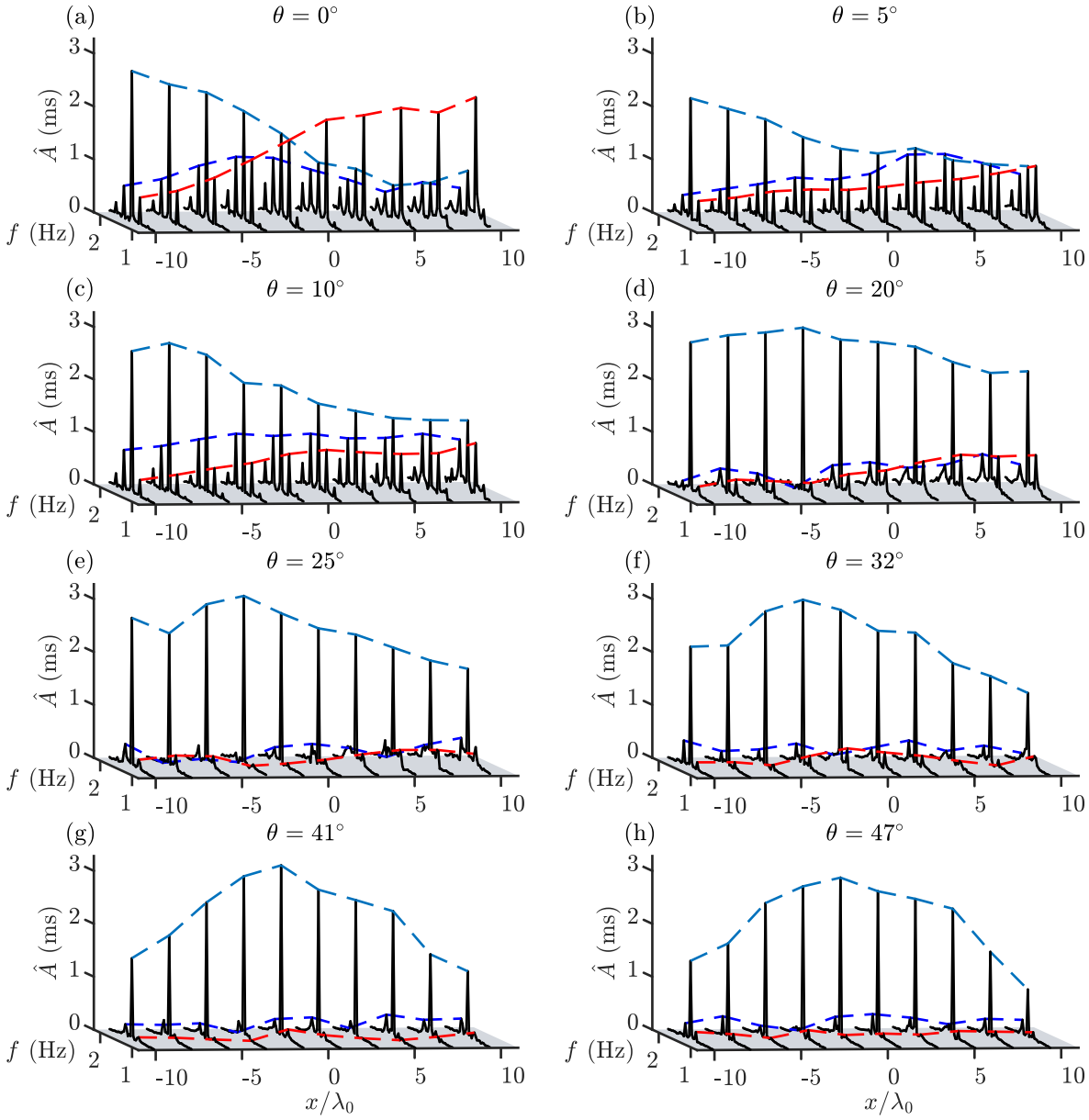

Figure 5. Amplitude spectra for experiments 2a-h (part II) obtained using the measured free surface time series along the primary wave propagation direction (see fig. 3a for gauge locations) for different crossing angles θ. Dashed lines follow the amplitudes of the carrier (light blue), lower sideband (red), and upper sideband (dark blue).

in amplitude within $13\lambda_0$. Figure 5a presents the amplitude spectra for experiment 2a. Substantial growth in secondary sidebands is evident. These secondary sideband frequency components, located at multiples of the perturbation frequency, contribute to the growth of wave group amplitudes and further enhance the strong decline of the carrier amplitude.

4.2. Crossing waves: $0° < \theta < 47°$

Figure 6b-d show that the growth observed in the unidirectional case continues but slows as the crossing angle is increased to 20°. In these experiments, the maximum amplification factor of the upper sideband generally reduces compared to the unidirectional case, whereas the upper sideband appears relatively unaffected, with no strong growth in either case. The pulse formations seen in experiment 2a persist in fig. 4b-d and fig. 5b-d, though with reduced magnitude. The unseeded carrier

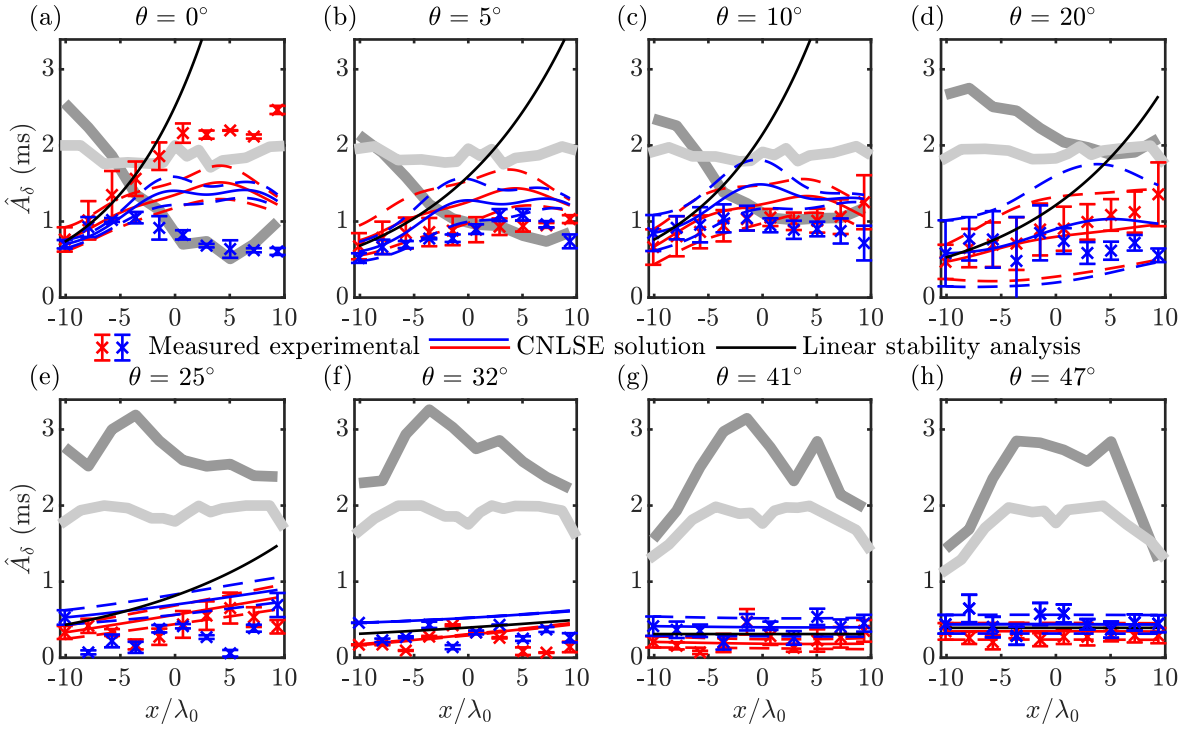

Figure 6. Comparison of the evolution of sideband amplitude along the centreline of the basin for experiments 2a-h (part II) from measurements, numerical solutions (crosses) of the CNLSE (thin blue and red lines) and linear stability analysis (thin black lines). Lower and upper sidebands are indicated in red and blue, respectively. Error bars and dashed lines represent one standard deviation from the mean across repeats for the measured data and the CNLSE solution, respectively. Thick lines represent the mean seeded (dark grey) and unseeded (light grey) carrier waves across repeats.

wave amplitude profiles of fig. 6b-d remain largely unchanged along the length of the basin, indicating that the effective length, over which crests reach their full amplitudes, is sufficiently long. Between $\theta = 25°$ and $\theta = 41°$ (fig. 6e-g), the transition to stability takes places. Experiments at angles of 41° and higher (fig. 6g-h, and appendix B for the measurements from experiments 2i-l) are stable.

5. Conclusion

We have experimentally investigated the effects of crossing angle on the modulational instability of two crossing nonlinear surface gravity wavetrains seeded with sideband perturbations and compared this to predictions by the the coupled nonlinear Schrödinger equation (CNLSE). The results demonstrate that sideband growth, as predicted by linear stability analysis of the CNLSE, can be reproduced in physical experiments undertaken in a circular wave basin. Strong modulation occurred in the unidirectional case, where the beginnings of recurrence were observed. The growth rate reduced as the crossing angle was increased; negligible growth was measured at and beyond a crossing angle of approximately 30°. Due to the reduced growth rate and the finite length of the basin, we have not been able to observe the increased amplification factors associated with angles approaching 35.26° [22,23]. An unseeded, regular wave was used to estimate the finite-crest effect (an experimental limitation for a finte-size round basin), which started to become significant at 42°, well beyond the theoretical stability boundary of 35.26°. Taking into account the reduction in evolution length imposed by the finite-crest effect, no growth in sidebands was found to occur at these high angles. Future work should seek to extend experimental measurements into the second (high- angle) unstable region. To complete this successfully, the finite-crest effect must be considered allowing sidebands enough interaction evolution distance to grow. We envisage this will be challenging in the FloWave basin.

Acknowledgements

The authors would like to thank Mr E. Nixon, Dr S. Draycott, and Dr T. Davey at FloWave for their help designing and carrying out the experiments. FloWave was funded by the UK EPSRC (EP/I02932X/1). JNS acknowledges an EPSRC studentship (No. 1770088), and TSvdB a Royal Academy of Engineering Research Fellowship.

Appendix A. Split-step time marching technique

The split-step method (also known as the Fourier method) takes advantage of the fact that the linear and nonlinear components can be separated and then solved exactly [49]. The linear component is solved in Fourier space, whereas the nonlinear is solved in the time or space domain. In the split-step method, the linear and nonlinear components of the CNLSEs are treated independently and the predictions combined immediately after each time step as the full solution advances forward. A known error of $\mathcal{O}(\epsilon^3)$ is associated with the independence assumption. The split-step method is second-order accurate in Δt and to all orders in Δx, it is unconditionally stable [50].

First, the CNLSE is rearranged and split into its linear and nonlinear components (here only (6) is considered for brevity),

$$\mathcal{L}: \frac{\partial A}{\partial t} = i\alpha \frac{\partial^2 A}{\partial x^2}, \quad \mathcal{N}: \frac{\partial A}{\partial t} = -i(\xi |A|^2 + 2\zeta |B|^2)A. \tag{A1}$$

The nonlinear component is integrated forwards in the time domain as follows,

$$A_{i+1} = A_i e^{-\Delta x i(\xi |A_i|^2 + 2\zeta |B_i|^2)}, \tag{A2}$$

whereas the linear component is Fourier-transformed,

$$\frac{\partial \hat{A}}{\partial t} = i\hat{A}\alpha(i\omega)^2, \tag{A3}$$

$$= -i\alpha\hat{A}\omega^2, \tag{A4}$$

and then integrated in time to give,

$$\hat{A}_{i+1} = \hat{A}_i e^{-\Delta x i\alpha\omega^2}. \tag{A5}$$

Combining the linear and nonlinear components, at each time step we have the explicit expression,

$$A_{i+1} = \mathcal{F}^{-1}\left(\hat{A}_i e^{-\Delta x i\alpha\omega^2} + \mathcal{F}\left(A_i e^{-\Delta x i(\xi |A_i|^2 + 2\zeta |B_i|^2)}\right)\right). \tag{A6}$$

Appendix B. Experiment 2j-l: $60^\circ < \theta < 88^\circ$

References

1. Bitner-Gregersen, E.; Gramstad, O. Rogue waves impact on ships and offshore structures. *Det Norske Veritas Germanischer Lloyd Strategic Research and Innovation Position Paper* **2015**.
2. Cavaleri, L.; Bertotti, L.; Torrisi, L.; Bitner-Gregersen, E.; Serio, M.; Onorato, M. Rogue waves in crossing seas: The Louis Majesty accident. *J. Geophys. Res. Oceans* **2012**, *117*.
3. Kharif, C.; Pelinovsky, E. Physical mechanisms of the rogue wave phenomenon. *Eur. J. Mech. B - Fluid* **2003**, *22*, 603–634.
4. Dysthe, K.; Krogstad, H.E.; Müller, P. Oceanic rogue waves. *Annu. Rev. Fluid Mech.* **2008**, *40*, 287–310.
5. Onorato, M.; Residori, S.; Bortolozzo, U.; Montina, A.; Arecchi, F. Rogue waves and their generating mechanisms in different physical contexts. *Phys. Rep.* **2013**, *528*, 47–89.
6. Adcock, T.A.; Taylor, P.H. The physics of anomalous ('rogue') ocean waves. *Rep. Prog. Phys.* **2014**, *77*, 105901.

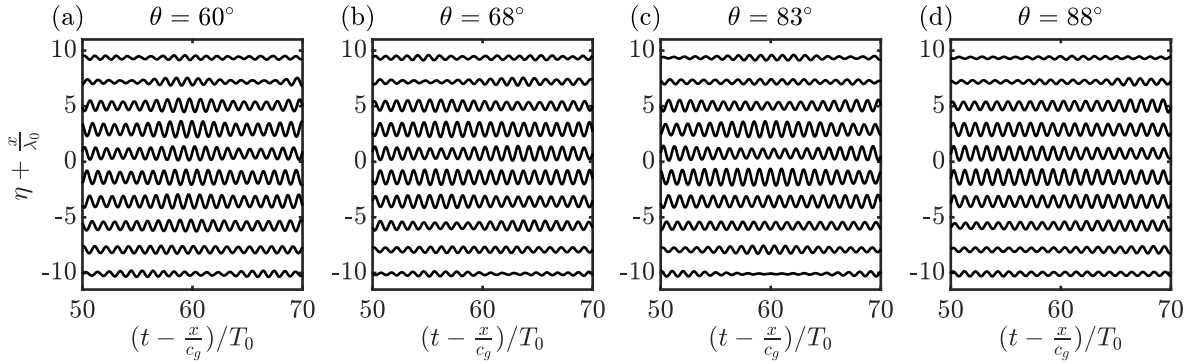

Figure A1. Measured free surface elevation time series for experiments 2i-l (part II) shifted by the linear group velocity $c_g = \sqrt{C_x^2 + C_y^2}$, with the positive vertical representing increasing distance along the basin.

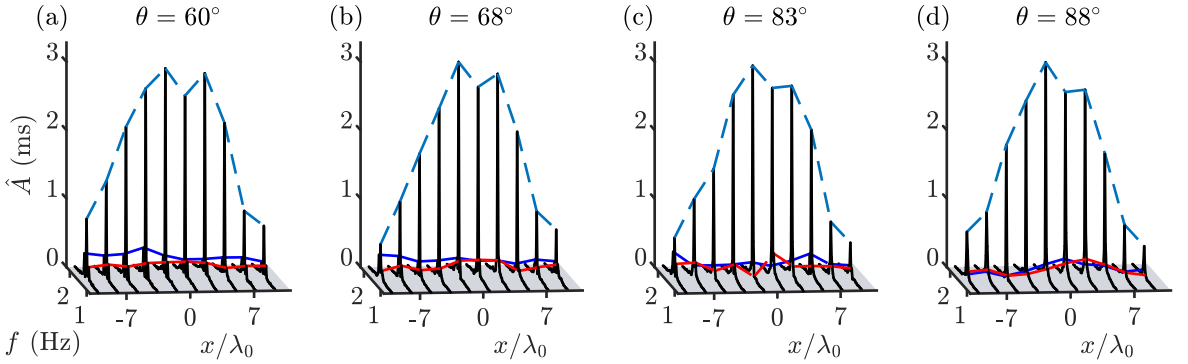

Figure A2. Amplitude spectra for experiments 2i-l (part II) obtained using the measured free surface time series along the primary wave propagation direction (see fig. 3a for gauge locations) for different crossing angles θ. Dashed lines follow the amplitudes of the carrier (light blue), lower sideband (red), and upper sideband (dark blue).

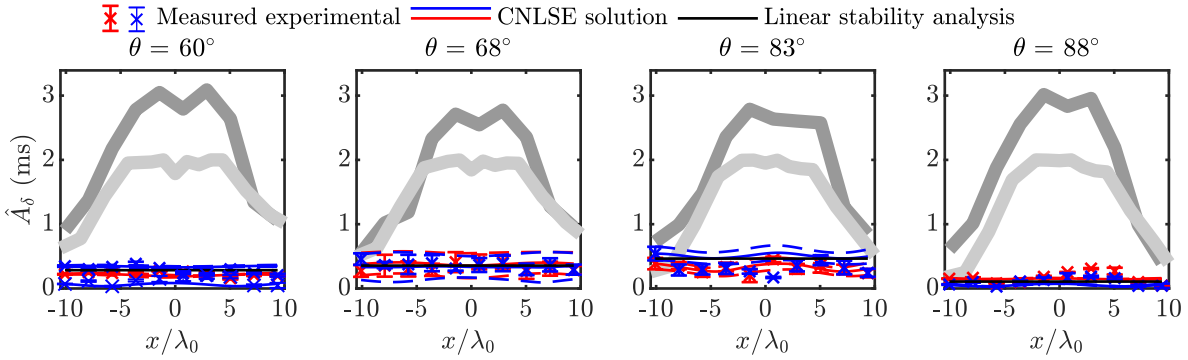

Figure A3. Comparison of the evolution of sideband amplitude along the centreline of the basin for experiments 2i-l (part II) from measurements, numerical solutions (crosses) of the CNLSE (thin blue and red lines) and linear stability analysis (thin black lines). Lower and upper sidebands are indicated in red and blue, respectively. Error bars and dashed lines represent one standard deviation from the mean across repeats for the measured data and the CNLSE solution, respectively. Thick lines represent the mean seeded (dark grey) and unseeded (light grey) carrier waves across repeats.

7. Yuen, H.C.; Lake, B.M. Nonlinear dynamics of deep-water gravity waves. In *Adv. Appl. Mech.*; Elsevier, 1982; Vol. 22, pp. 67–229.
8. Benjamin, T.B.; Feir, J. The disintegration of wave trains on deep water Part 1. Theory. *J. Fluid Mech.* **1967**, *27*, 417–430.

9. Ma, Y.C. The perturbed plane-wave solutions of the cubic Schrödinger equation. *Stud, Appl. Math.* **1979**, *60*, 43–58.
10. Peregrine, D.H. Water waves, nonlinear Schrödinger equations and their solutions. *ANZIAM J.* **1983**, *25*, 16–43.
11. Akhmediev, N.; Ankiewicz, A.; Taki, M. Waves that appear from nowhere and disappear without a trace. *Phys. Lett. A* **2009**, *373*, 675–678.
12. Chabchoub, A.; Hoffmann, N.; Onorato, M.; Akhmediev, N. Super rogue waves: observation of a higher-order breather in water waves. *Phys. Rev. X* **2012**, *2*, 011015.
13. Chabchoub, A.; Hoffmann, N.; Akhmediev, N. Rogue wave observation in a water wave tank. *Phys. Rev. Lett.* **2011**, *106*, 204502.
14. Lake, B.M.; Yuen, H.C.; Rungaldier, H.; Ferguson, W.E. Nonlinear deep-water waves: theory and experiment. Part 2. Evolution of a continuous wave train. *J. Fluid Mech.* **1977**, *83*, 49–74.
15. Fermi, E.; Pasta, P.; Ulam, S.; Tsingou, M. Studies of the nonlinear problems. Technical report, Los Alamos Scientific Lab., N. Mex., 1955.
16. Ford, J. The Fermi-Pasta-Ulam problem: paradox turns discovery. *Phys. Rep.* **1992**, *213*, 271–310.
17. Janssen, P.A.E.M. Modulational instability and the Fermi-Pasta-Ulam recurrence. *Phys. Fluids* **1981**, *24*, 23–26.
18. Onorato, M.; Osborne, A.R.; Serio, M. Modulational instability in crossing sea states: A possible mechanism for the formation of freak waves. *Phys. Rev. Lett.* **2006**, *96*, 014503.
19. Zakharov, V.E. Stability of periodic waves of finite amplitude on the surface of a deep fluid. *J. Appl. Mech. Tech. Phy.* **1968**, *9*, 190–194.
20. Hammack, J.L.; Henderson, D.M.; Segur, H. Progressive waves with persistent two-dimensional surface patterns in deep water. *J. Fluid Mech.* **2005**, *532*, 1–52.
21. Ruban, V. Giant waves in weakly crossing sea states. *J. Exp. Theor. Phys.*+ **2010**, *110*, 529–536.
22. Onorato, M.; Proment, D.; Toffoli, A. Freak waves in crossing seas. *Eur. Phys. J. - Spec. Top.* **2010**, *185*, 45–55.
23. Ablowitz, M.J.; Horikis, T.P. Interacting nonlinear wave envelopes and rogue wave formation in deep water. *Phys. Fluid.* **2015**, *27*, 012107.
24. Toffoli, A.; Fernandez, L.; Monbaliu, J.; Benoit, M.; Gagnaire-Renou, E.; Lefevre, J.; Cavaleri, L.; Proment, D.; Pakozdi, C.; Stansberg, C.; others. Experimental evidence of the modulation of a plane wave to oblique perturbations and generation of rogue waves in finite water depth. *Phys. Fluids* **2013**, *25*, 091701.
25. Toffoli, A.; Bitner-Gregersen, E.M.; Osborne, A.R.; Serio, M.; Monbaliu, J.; Onorato, M. Extreme waves in random crossing seas: Laboratory experiments and numerical simulations. *Geophys. Res. Lett.* **2011**, *38*.
26. Chabchoub, A.; Mozumi, K.; Hoffman, N.; Babanin, A.V.; Toffoli, A.; Steer, J.N.; van den Bremer T. S..; Akhmediev, N.; Onorato, M.; Waseda, T. Observation of short-crested slanted solitons and breathers. *P. Natl. A. Sci. USA (forthcoming)* **2019**, -, –.
27. Okihiro, M.; Guza, R.T.; Seymour, R.J. Bound infra-gravity waves. *J. Geophys. Res.* **1992**, *97*, 453–469.
28. Herbers, T.H.C.; Elgar, S.; Guza, R.T. Infragravity-frequency (0.005-0.05 Hz) motions on the shelf. Part I: Forced waves. *J. Phys. Oceanogr.* **1994**, *24*, 917–927.
29. Toffoli, A.; Onorato, M.; Monbaliu, J. Wave statistics in unimodal and bimodal seas from a second-order model. *Eur. J. Mech. B-Fluid.* **2006**, *25*, 649–661.
30. Christou, M.; Tromans, P.; Vanderschuren, L.; Ewans, K. Second-order crest statistics of realistic sea states. Proc. of the 11th Int. Workshop on Wave Hindcasting and Forecasting, Halifax, Canada, 2009, pp. 18–23.
31. Hasselmann, K. On the non-linear energy transfer in a gravity-wave spectrum Part 1. General theory. *J. Fluid Mech.* **1962**, *12*, 481–500.
32. Sharma, J.N.; Dean, R.G. Second-order directional seas and associated wave forces. *Soc. Petrol. Eng. J.* **1981**, *21*, 129–140.
33. Dalzell, J.F. A note on finite depth second-order wave–wave interactions. *App. Ocean Res.* **1999**, *21*, 105–111.
34. Forristall, G.Z. Wave crest distributions: Observations and second-order theory. *J. Phys. Oceanogr.* **2000**, *30*, 1931–1943.
35. Walker, D.A.G.; Taylor, P.H.; Eatock Taylor, R. The shape of large surface waves on the open sea and the Draupner New Year wave. *App. Ocean Res.* **2004**, *26*, 73–83.

36. Toffoli, A.; Monbaliu, J.; Onorato, M.; Osborne, A.R.; Babanin, A.V.; Bitner-Gregersen, E.M. Second-order theory and setup in surface gravity waves: a comparison with experimental data. *J. Phys. Oceanogr.* **2007**, *37*, 2726–2739.
37. Santo, H.; Taylor, P.H.; Eatock Taylor, R.; Choo, Y.S. Average properties of the largest waves in Hurricane Camille. *Journal of Offshore Mechanics and Arctic Engineering* **2013**, *135*, 011602.
38. McAllister, M.L.; Adcock, T.A.A.; Taylor, P.H.; van den Bremer, T.S. The set-down and set-up of directionally spread and crossing surface gravity wave groups. *J. Fluid Mech.* **2018**, *835*, 131–169.
39. Haver, S. A possible freak wave event measured at the Draupner jacket January 1 1995. Rogue Waves Workshop; , 2004; pp. 1–8.
40. Adcock, T.; Taylor, P.; Yan, S.; Ma, Q.; Janssen, P. Did the Draupner wave occur in a crossing sea? *P. Roy. Soc. A* **2011**, *467*, 3004–3021.
41. McAllister, M.L.; Draycott, S.; Adcock, T.A.A.; Taylor, P.H.; van den Bremer, T.S. Laboratory recreation of the Draupner wave and the role of breaking in crossing seas. *J. Fluid Mech.* **2019**, *860*, 767–786.
42. Fedele, F.; Brennan, J.; De León, S.P.; Dudley, J.; Dias, F. Real world ocean rogue waves explained without the modulational instability. *Scientific Reports* **2016**, *6*, 27715.
43. Brennan, J.; Dudley, J.M.; Dias, F. Extreme waves in crossing sea states. *Int. J. Ocean Coast. Eng.* **2018**, *1*, 1850001.
44. Støle-Hentschel, S.; Trulsen, K.; Rye, L.B.; Raustøl, A. Extreme wave statistics of counter-propagating, irregular, long-crested sea states. *Phys. Fluids* **2018**, *30*, 067102.
45. Gramstad, O.; Bitner-Gregersen, E.; Trulsen, K.; Nieto Borge, J.C. Modulational instability and rogue waves in crossing sea states. *J. Phys. Oceanogr.* **2018**, *48*, 1317–1331.
46. Noble, D.R. Combined wave-current scale model testing at FloWave. *EngD* **2017**.
47. Dysthe, K.B.; Trulsen, K.; Krogstad, H.E.; Socquet-Juglard, H. Evolution of a narrow-band spectrum of random surface gravity waves. *Journal of Fluid Mechanics* **2003**, *478*, 1–10.
48. Melville, W. The instability and breaking of deep-water waves. *Journal of Fluid Mechanics* **1982**, *115*, 165–185.
49. Weideman, J.; Herbst, B. Split-step methods for the solution of the nonlinear Schrödinger equation. *SIAM J. Numer. Anal.* **1986**, *23*, 485–507.
50. Taha, T.R.; Ablowitz, M.I. Analytical and numerical aspects of certain nonlinear evolution equations. II. Numerical, nonlinear Schrödinger equation. *J. Comput. Phys.* **1984**, *55*, 203–230.